

See discussions, stats, and author profiles for this publication at: <https://www.researchgate.net/publication/274644652>

Bone enhancement in ultrasound using local spectrum variations for guiding percutaneous scaphoid fracture fixation...

Article in *International Journal of Computer Assisted Radiology and Surgery* · April 2015

DOI: 10.1007/s11548-015-1181-6 · Source: PubMed

CITATIONS

5

READS

65

12 authors, including:



Emran Mohammad Abu Anas

University of British Columbia - Vancouver

21 PUBLICATIONS 131 CITATIONS

[SEE PROFILE](#)



Alexander Seitel

German Cancer Research Center

104 PUBLICATIONS 754 CITATIONS

[SEE PROFILE](#)



Abtin Rasoulia

University of British Columbia - Vancouver

41 PUBLICATIONS 293 CITATIONS

[SEE PROFILE](#)



David Pichora

Kingston General Hospital

64 PUBLICATIONS 919 CITATIONS

[SEE PROFILE](#)

Some of the authors of this publication are also working on these related projects:



Phenol-based Soft Embalming [View project](#)



EM-Tracked Personalized Guides [View project](#)

Bone enhancement in ultrasound using local spectrum variations for guiding percutaneous scaphoid fracture fixation procedures

Emran Mohammad Abu Anas¹ · Alexander Seitel¹ · Abtin Rasoulia¹ · Paul St. John² · David Pichora² · Kathryn Darras³ · David Wilson⁴ · Victoria A. Lessoway⁵ · Ilker Hacihaliloglu⁶ · Parvin Mousavi⁷ · Robert Rohling^{1,8} · Purang Abolmaesumi¹

Received: 5 March 2015 / Accepted: 17 March 2015 / Published online: 7 April 2015
© CARS 2015

Abstract

Purpose The scaphoid bone is the most frequently fractured bone in the wrist. When fracture fixation is indicated, a screw is inserted into the bone either in an open surgical procedure or percutaneously under fluoroscopic guidance. Due to the complex geometry of the wrist, fracture fixation is a challenging task. Fluoroscopic guidance exposes both the patient and the physician to ionizing radiation. Ultrasound-based guidance has been suggested as a real-time, radiation-free alternative. The main challenge of using ultrasound is the difficulty in interpreting the images due to the low contrast and noisy nature of the data.

We would like to thank the Natural Sciences and Engineering Research Council (NSERC) and the Canadian Institutes of Health Research (CIHR) for funding this project.

✉ Emran Mohammad Abu Anas
emrana@ece.ubc.ca
Purang Abolmaesumi
purang@ece.ubc.ca

- ¹ Electrical and Computer Engineering, University of British Columbia, Vancouver, BC, Canada
- ² Kingston General Hospital, Kingston, ON, Canada
- ³ Vancouver General Hospital, Vancouver, BC, Canada
- ⁴ Department of Orthopaedics, Centre for Hip Health and Mobility, University of British Columbia, Vancouver, BC, Canada
- ⁵ BC Women's Hospital, Vancouver, BC, Canada
- ⁶ Biomedical Engineering, Rutgers-The State University of New Jersey, New Brunswick, NJ, USA
- ⁷ Kingston School of Computing, Queen's University, Kingston, ON, Canada
- ⁸ Mechanical Engineering, University of British Columbia, Vancouver, BC, Canada

Methods We propose a bone enhancement method that exploits local spectrum features of the ultrasound image. These features are utilized to design a set of quadrature band-pass filters and subsequently estimate the local phase symmetry, where high symmetry is expected at the bone locations. We incorporate the shadow information below the bone surfaces to further enhance the bone responses. The extracted bone surfaces are then used to register a statistical wrist model to ultrasound volumes, allowing the localization and interpretation of the scaphoid bone in the volumes.

Results Feasibility experiments were performed using phantom and in vivo data. For phantoms, we obtain a surface distance error 1.08 mm and an angular deviation from the main axis of the scaphoid bone smaller than 5°, which are better compared to previously presented approaches.

Conclusion The results are promising for further development of a surgical guidance system to enable accurate anatomy localization for guiding percutaneous scaphoid fracture fixations.

Keywords Ultrasound bone enhancement · Scaphoid fracture · Phase symmetry · Wrist model

Introduction

Wrist injuries are the most common injuries originating from work- and sport-related accidents accounting for more than 250,000 cases annually only in North America [18, 24]. Among all carpal bones, the scaphoid bone is the most fractured bone, representing about 90 % of all carpal fractures [22]. For non-displaced fracture cases, treatment involves immobilization of the wrist in a short arm cast. The typical recovery time ideally accounts for 10–12 weeks but can be extended, e.g., when the fracture causes disrupted

blood supply to the scaphoid bone. In cases where the proximal pole (the part closest to the forearm) is affected by the fracture, immobilization itself may not be sufficient for treatment as the healing time is often extended to 18–20 weeks [22], and there is an increased risk that parts of the bones even die. For these cases, clinicians suggest surgery to avoid later complications such as wrist arthritis. The scaphoid bone is then fixated by inserting a screw along its central longitudinal axis. This screw insertion is difficult because it has to be performed in close vicinity to the surrounding wrist bones and their cartilages, where a violation damages the surrounding joints. Thus, surgical accuracy for these procedures should be <2 mm [19]. Conventionally, the fixation is done in an open surgical approach because it allows accurate placement of the screw. However, open surgery often leads to the risk of damaging soft tissue, destabilizes important ligament attachments, compromises the blood supply and increases the risk of infections.

To reduce most of these risks, percutaneous approaches have been proposed [20]. However, they are mostly performed under 2D fluoroscopic guidance which renders a more accurate screw insertion difficult because the complex 3D geometry is hard to interpret on the 2D radiographic projections [29]. Though the amount of dose is negligible in this kind of peripheral procedures, the staff members frequently working in the operating room may be affected by the X-ray radiation as a long-term effect. To address these drawbacks, ultrasound (US) guidance has been suggested as an alternative [2]. Advantages of US include the ability to acquire 3D volumes in real time, without ionizing radiation, relatively low cost and easy of use. US images acquired during the intervention can also be registered to a preoperative CT [25] or a statistical model [13] for additional guidance. Beek et al. [2] explored the feasibility of accurate screw insertions by registering manually segmented surfaces of the scaphoid bone from preoperative wrist CT to intraoperative US images. The main drawbacks of their method include the challenging registration given the smooth featureless surface of the scaphoid bone and the mandatory, labor intensive manual bone segmentation.

Apart from the scaphoid fracture fixation systems, US-based approaches have been proposed in many other computer-assisted orthopedic surgical applications [1, 3, 15, 25, 30, 31]. The main challenge of these approaches is the detection/enhancement of the bone surface in the noisy US image. Penney et al. [25] proposed to enhance the pixel response of the bony parts in the US image by defining a measure based on the pixel intensity and the ratio of the number of zero pixels between the pixel of interest and the last pixel of the corresponding column to the total number of pixels between them. Both measurements were expected to have high values for the bony part because of the large change in acoustic impedances between soft tissue and bone. Amin

et al. [1] used a directional edge detector to detect the transition between the bone shadow region and the bone surface reflection. They found the pixels greater than an empirically set bone surface threshold in each column along the upward direction. The output of the directional edge was convolved with a Gaussian kernel to ensure that the edge detector region captured the entire bone surface reflection. Yan et al. [31] used a backward tracing method that was similar to the directional edge detector, except the idea was based on a fan-shaped sector of the phased array probe. Kowal et al. [15] presented an automatic US bone contour detection approach that was subdivided into two main steps. Firstly, they identified a sub-image range that most likely contained the bony part in the US image. Then, they searched for the bone contour within the sub-image region. Foroughi et al. [4] modeled the shadow below a pixel that belongs to the bony part of the US image as a Gaussian weighting function and subsequently calculated a bone probability map in an US image. They then proposed a cost function that includes continuity and smoothness of the bone surface, and dynamic programming was used for finding the global minima in order to detect the bone contour. However, the main challenge of all of the described intensity-based bone contour detection approaches is the sensitivity of their methods to US artifacts and machine settings [9, 11]. For example, the assumption of high-intensity values along the bone region is not always true, particularly when the US transducer is not positioned perpendicular to the bone surface. This issue is often noticed for curved wrist bone surfaces, which in turn leads to low-contrast, blurred and disconnected bone features [12].

To address the above-mentioned challenges, local phase-based US image enhancement approaches were recently suggested. They were reported for bone enhancement [8–11] as well as localizing soft tissue interfaces [7, 26, 27]. In the local phase-based approach, the phase symmetry (PS) information was utilized to detect the ridge-like features in US images, using a set of quadrature filters at different scales and orientations. Hacıhaliloglu et al. [8] used Log-Gabor filters to obtain the PS information from a 2D US image that showed high values at the expected bone locations. The same authors extended their 2D approach to 3D US by designing 3D Log-Gabor filters [10]. Most recently, Hacıhaliloglu et al. [11] proposed a local phase tensor metric for enhancing bone features in US images. The tensor was computed using an isotropic band-pass (Log-Gabor) filtered image, its gradient and Hessian. The filter parameters (scale, bandwidth, orientation and angular bandwidth of the filter) were estimated from the image content by incorporating the principal curvature computed from the Hessian matrix and directional filter banks in a phase scale-space framework [10]. The filter design considered an isotropic scale and bandwidth of the filters at all orientations, i.e., the frequency responses of the

filters are the same throughout all orientations. However, the frequency response of a curved surface in US shows variations over different orientations. As a result, this approach may not detect/enhance this kind of surface without accounting for the spectrum variations over different orientations.

In this paper, we propose a new technique for enhancing bone surfaces in US images based on an empirical wavelet approach that exploits the local spectrum variation of the ultrasound image. Empirical wavelet filters have been proposed in the literature to extract the different modes of a signal according to its contained information [5,6]. We propose to account for the local spectrum variations to be able to design a filter bank for subsequent local PS estimation. Bone shadow information is also utilized to better differentiate the bone surface from the soft tissue, nerves and other anatomies in US images. For evaluation, we apply the proposed approach in our previously presented registration framework [28] where a statistical wrist model is registered to US volumes to allow for augmentation of the wrist bone surfaces onto the US images. The statistical wrist model was developed by our group [21]; it captures the major modes of shape and pose variations across 30 subjects at different wrist positions. Both phantom and in vivo data are acquired for the feasibility experiments. The registration accuracy is determined for the wrist phantoms in comparison with the methods proposed in [8,11].

Methods

We first present our proposed bone enhancement approach for US images, and then, we demonstrate how the enhancement enables registration of a statistical wrist model to the US data.

Bone detection

A bone surface in an US image produces highest intensity values when the US beam falls perpendicularly to that bone surface; otherwise, the response from that bone surface will be weaker. Since an US signal cannot propagate through the bony structure due to the large mismatches in acoustic impedances between the bone and neighboring tissues, shadows are observed below the bone surfaces. The bone response above the shadow has a certain width, can reach up to 4 mm [12]. In addition, blurred and disconnected bone responses are also often observed.

To accommodate these characteristics of bone US imaging and still aim for an improved detection of bone surfaces, we propose an approach that is based on the idea of local PS as introduced in [8,14]. Typically, local PS shows high magnitudes at the expected bone locations as well as other features

in US images [8]. For estimation of the local PS, a set of quadrature filters at different scales and different orientations are used. A quadrature filter in 2D has two components, one represents the frequency response along the radial direction, the other across the azimuthal direction. Mathematically, the frequency response ($F(\omega, \phi)$) of a quadrature filter at scale $s(1 \leq s \leq S)$ and orientation $o(1 \leq o \leq O)$ can be expressed as:

$$F_{s,o}(\omega, \phi) = R_{s,o}(\omega)G_{s,o}(\phi), \quad (1)$$

where ω and ϕ are the polar domain coordinates, *radius* and *azimuth*, respectively, of the 2D frequency response. The radial component ($R_{s,o}(\omega)$) determines the frequency band, and the angular component ($G_{s,o}(\phi)$) controls the orientation of the frequency response in the 2D domain. S and O are the total number of scales and orientations, respectively.

In previous works [8,9,11], the parameters of $R_{s,o}(\omega)$ were assumed constant at different orientations over all slices in an US volume, which may not be optimal, because it does not account for local spectrum variations. To understand the variation of frequency responses over the spectrum, we present some examples of 2D Fourier spectrums of idealized bone-like responses. Figure 1a–c shows three images representing a horizontal line, an inclined line and a curved structure. The corresponding 2D Fourier magnitude spectrums are demonstrated in Fig. 1d–f on a logarithmic scale. We notice that a horizontal structure in the image domain produces a response along the vertical axis in the Fourier domain. In addition, the width of the response is different in the horizontal and vertical directions, and the width along the vertical direction is significantly greater than that along the horizontal direction. An inclined line such as in Fig. 1b also produces an inclined line-like structure in the Fourier domain. It is worth noting that the Fourier spectrum of Fig. 1b is rotated with respect to that of Fig. 1c by the same angle difference between the inclined and the horizontal lines. Here, most of the energy is concentrated along the inclined major axis. Finally, a curved structure in the spatial domain also creates a curved-like structure in the Fourier domain, and the zero crossings of the lobes are not located along a circle's trajectory. Moreover, the energy is more spread out in the Fourier domain compared to the line-like structure.

The above examples reveal that the energy of the Fourier spectrum distributes non-uniformly all over the region. Furthermore, the width of the lobe is different in different directions. Our proposed approach accounts for the local spectrum variation by using filters with appropriate parameters at different orientations. In the following, we will present the different steps of our proposed bone enhancement method which are illustrated in the flowchart shown in Fig. 2. Note that the approach is proposed for a 3D US volume, and it

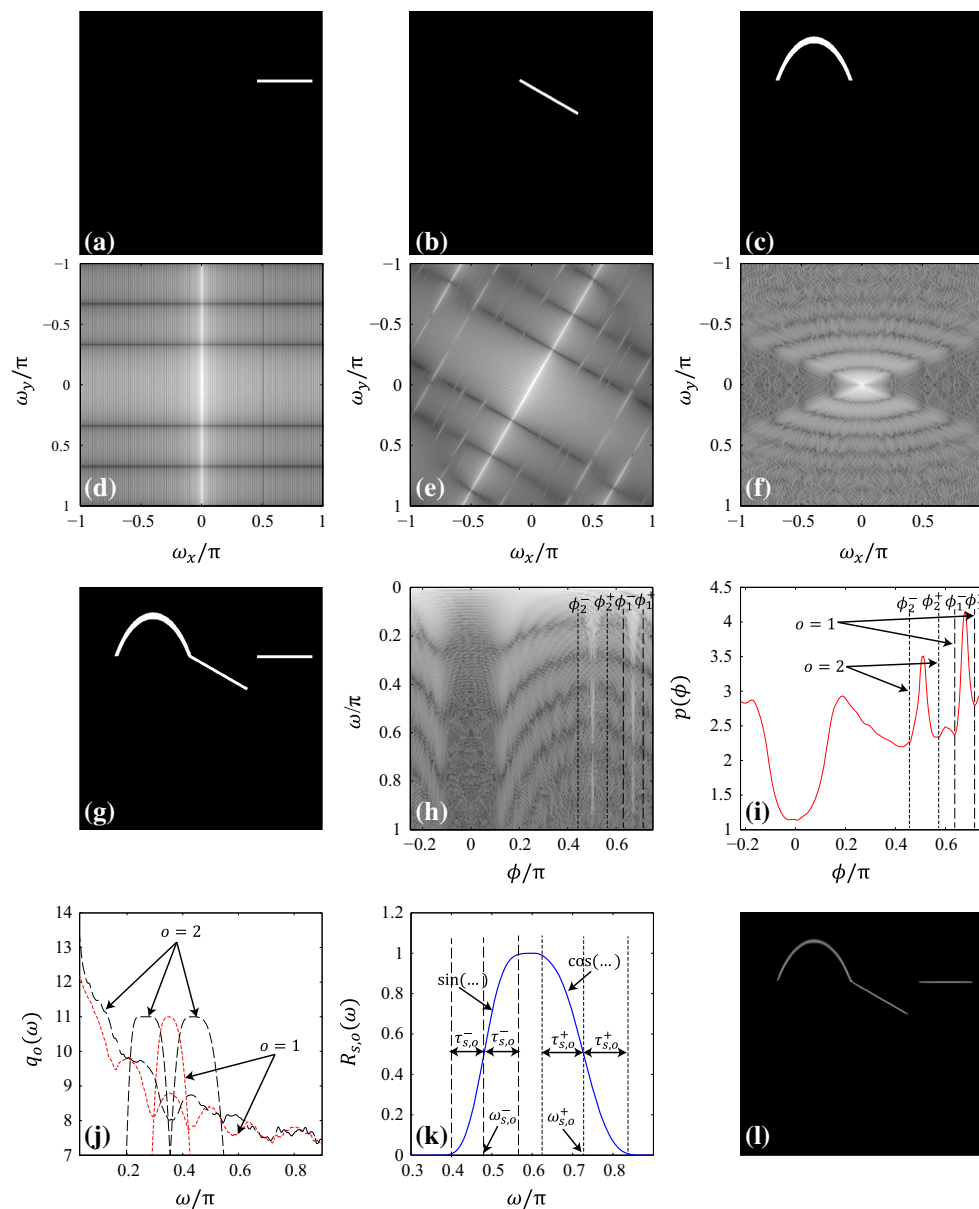


Fig. 1 Simulated US bone responses and their spectra. **a–c** Three simulated bone responses, **d–f** corresponding 2D Fourier transformations. **g** Summation of the three individual simulated images. **h** Fourier magnitude transform $\log(|P(\omega, \phi)|)$ of **g** in polar domain. **i** Variation of $p(\phi)$ (see Eq. 2) over ϕ . Two segmented portions are marked by $o = 1$

and $o = 2$. **j** Variation of $q_o(\omega)$ over ω for orientation index $o = 1$ and $o = 2$. Some filter responses are also demonstrated for $o = 1$ and $o = 2$. **k** Frequency response of the radial component of the band-pass quadrature filter. **l** Estimated PS image for the simulated US image in **g**

can be acquired by sweeping a US transducer over a region of interest, either with motorized transducer or with tracked transducer.

Calculation of the polar Fourier transform

For designing the filters, we use the polar Fourier transform instead of the conventional Fourier transform computed over a rectangular grid, because the parameters of the quadrature filters are directly related to the coordinates of the polar

domain. Let $U_k(x, y)$ be the input US image, and $P_k(\omega, \phi)$ be the corresponding Fourier transform in polar domain, where $\omega_1 \leq \omega \leq \omega_{N_\omega}$ and $\phi_1 \leq \phi \leq \phi_{N_\phi}$. N_ω and N_ϕ represent the number of radius and azimuthal bins in the polar Fourier transform. Initially, we select the first frame as a reference (r) frame ($P_r(\omega, \phi) = P_1(\omega, \phi)$). An example US image obtained by adding the three test images (Fig. 1a–c) is shown in Fig. 1g, and the magnitude (logarithmic scale) of the corresponding polar Fourier transform is demonstrated in Fig. 1h.

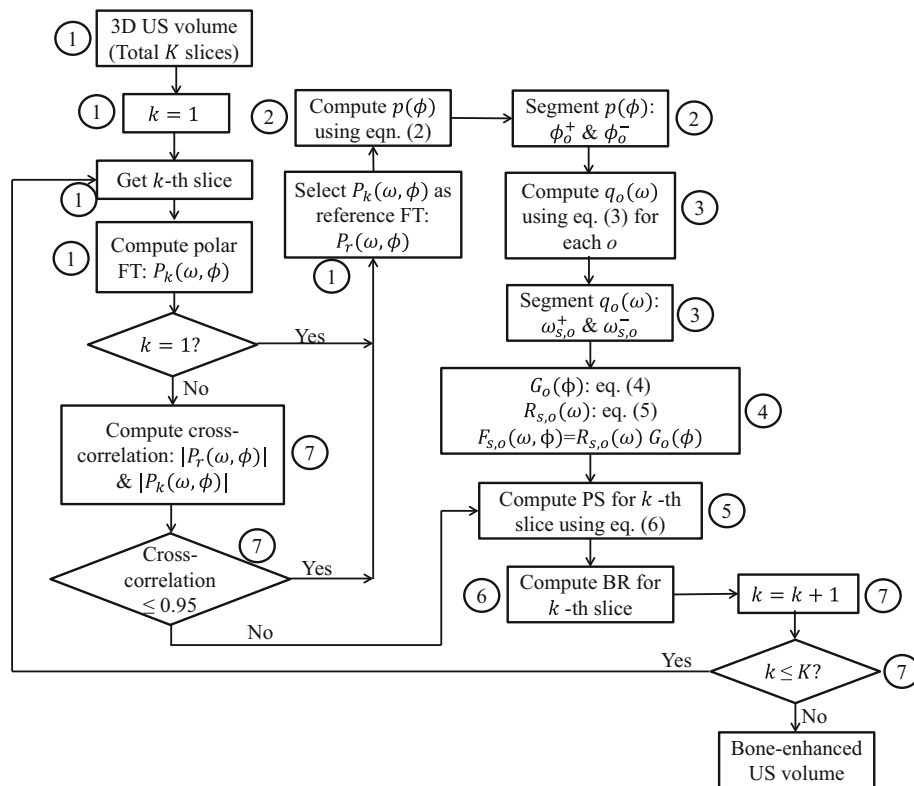


Fig. 2 The flowchart of the proposed bone enhancement approach. (1) The first frame of the K frames of the acquired US volume is selected, and the corresponding Fourier transform $P_k(\omega, \phi)$ in the polar domain is computed. Initially, the first frame is selected as the reference. (2) $p(\phi)$ is calculated using Eq. (2) and segmented to determine ϕ_o^+ and ϕ_o^- . (3) After that, $q_o(\omega)$ is determined for each orientation o using Eq. (3) and again segmented to determine $\omega_{s,o}^+$ and $\omega_{s,o}^-$. (4) The segmented supports are used in the designing filters, $G_o(\phi)$ using Eq. (4) and $R_{s,o}(\omega)$ using Eq. (5). (5) The local PS is computed using Eq. (6).

(6) After that, we obtain BR image from PS using the approach proposed by Foroughi et al. [4]. (7) For the next US frame, we discard the estimation of the filter parameters if the cross-correlation between the Fourier magnitude transform of that frame and that of the previously selected reference frame is > 0.95 . Otherwise, we again compute the filter parameters based on the Fourier transform of the selected US frame, and it is considered as the new reference. The process is continued until we reach to the last frame of the US volume, and in the end, we obtain collections of BR images from all US frames in the US volume

Parameter estimation for the angular filters

For estimation of the parameters of the angular filters $G_{s,o}(\phi)$, we average the logarithmic magnitude of $P_k(\omega, \phi)$ over ω ,

$$p(\phi) = \frac{1}{N_\omega} \sum_{\omega=\omega_1}^{\omega_{N_\omega}} \log(|P_k(\omega, \phi)|), \quad (2)$$

where a higher value in $p(\phi)$ indicates the presence of high energy at that particular orientation (Fig. 1i). To segment $p(\phi)$, we use the idea proposed in [6]. The segmented portions of $p(\phi)$ correspond to different orientations of the filter, i.e., the total number of orientations, (O), is equal to the number of segmented portions. Each separate portion is centered around a specific angular value (a maximum), and two neighboring supports/boundaries (minima or sufficient low magnitude) represented as ϕ_o^+ and ϕ_o^- (example supports are

shown in Fig. 1i). These values will be subsequently used for angular filter design.

Parameter estimation for the radial filters

In contrast to the previously published approaches [8, 9, 11], the parameters of the radial direction filters for each different orientation are computed separately. For each orientation o , we compute the average of the logarithmic magnitude of $P_k(\omega, \phi)$ over ϕ within that orientation range (ϕ_o^- to ϕ_o^+),

$$q_o(\omega) = \frac{1}{N_\phi^o} \sum_{\phi=\phi_o^-}^{\phi_o^+} \log(|P_k(\omega, \phi)|), \quad (3)$$

where N_ϕ^o is the number of angle bins within ϕ_o^- and ϕ_o^+ . Figure 1j shows $q_o(\omega)$ for two different segmented orientations, $o = 1, 2$, marked as corresponding orientations in Fig. 1i. We notice that the responses ($q_o(\omega)$) are quite differ-

ent for different orientations. This is expected, because the Fourier transform inside the segmented portion for $o = 1$ is relatively different from that for $o = 2$ (Fig. 1h). To estimate the parameters of the radial components of the filter, we segment $q_o(\omega)$. Let the neighboring radial supports for a particular orientation o be $\omega_{s,o}^-$ and $\omega_{s,o}^+$, and the total number of segmented portions of $q_o(\omega)$ be equal to the total number of scales in that particular orientation. Note that the leftmost segmented portion must not include the dc (zero frequency) value, because the quadrature filter has a condition of the dc value to be zero. We set the leftmost frequency to 0.02π , i.e., $\omega_{s,o}^- = 0.02\pi$ for $s = 1$ and all o .

Angular and radial filters

The angular component $G_o(\phi)$ for a particular orientation o can be expressed as:

$$G_o(\phi) = \begin{cases} 1, & \text{if } \phi_o^- + \delta_o^- \leq \phi \leq \phi_o^+ - \delta_o^+ \\ \cos \left[\frac{\pi}{2} \beta \left(\frac{1}{2\gamma\phi_o^+} (\phi - (1-\gamma)\phi_o^+) \right) \right], & \text{if } \phi_o^+ - \delta_o^+ \leq \phi \leq \phi_o^+ + \delta_o^+ \\ \sin \left[\frac{\pi}{2} \beta \left(\frac{1}{2\gamma\phi_o^-} (\phi - (1-\gamma)\phi_o^-) \right) \right], & \text{if } \phi_o^- - \delta_o^- \leq \phi \leq \phi_o^- + \delta_o^- \\ 0, & \text{otherwise,} \end{cases} \quad (4)$$

where $\delta_o^+ = \gamma\phi_o^+$ and $\delta_o^- = \gamma\phi_o^-$. The parameter γ relates to the transition of the frequency response, and we set it to 0.15. It ensures sufficiently sharp transitions of the frequency responses and minimizes the overlaps between them. The parameter x in $\beta(x)$ is defined in the above equation such that $0 \leq x \leq 1$. $\beta(x)$ is a function that satisfies the condition: $\beta(x) + \beta(1-x) = 1$ for $x \in [0, 1]$. Many functions satisfy these properties; however, the most common one used in the literature is $\beta = x^4(35 - 84x + 70x^2 - 20x^3)$ [5].

The frequency response $R_{s,o}(\omega)$ for a particular scale s at a particular orientation o can then be expressed as:

$$R_{s,o}(\omega) = \begin{cases} 1, & \text{if } \omega_{s,o}^- + \tau_{s,o}^- \leq \omega \leq \omega_{s,o}^+ - \tau_{s,o}^+ \\ \cos \left[\frac{\pi}{2} \beta \left(\frac{1}{2\gamma\omega_{s,o}^+} (\omega - (1-\gamma)\omega_{s,o}^+) \right) \right], & \text{if } \omega_{s,o}^+ - \tau_{s,o}^+ \leq \omega \leq \omega_{s,o}^+ + \tau_{s,o}^+ \\ \sin \left[\frac{\pi}{2} \beta \left(\frac{1}{2\gamma\omega_{s,o}^-} (\omega - (1-\gamma)\omega_{s,o}^-) \right) \right], & \text{if } \omega_{s,o}^- - \tau_{s,o}^- \leq \omega \leq \omega_{s,o}^- + \tau_{s,o}^- \\ 0, & \text{otherwise,} \end{cases} \quad (5)$$

where $\tau_{s,o}^+ = \gamma\omega_{s,o}^+$ and $\tau_{s,o}^- = \gamma\omega_{s,o}^-$. Figure 1k shows a sample frequency response, and the parameters are marked in the figure for understanding the above equation. In addition to designing filters at each orientation, we construct a special filter that has two neighboring supports of minimum and maximum frequencies in the detected segmented portions. For example, if the first scale ($s = 1$) represents the

leftmost segmented portion and the last scale ($s = S$) indicates the rightmost segmented one at orientation o , then the two neighboring supports of the special filter are $\omega_{1,o}^-$ and $\omega_{S,o}^+$. These special filters will be subsequently used for noise compensation in PS estimation.

To understand the reason behind different $R_{s,o}(\omega)$ over different orientations, consider the radial components for two orientations $o = 1$ and $o = 2$ in Fig. 1i. One of the peaks of $q_o(\omega)$ for $o = 1$ falls close to one of the minima of $q_o(\omega)$ for $o = 2$. In previous works [8,9,11], radial filters were designed with the same cutoff and center frequencies at different orientations. However, it is obvious in this figure that if we design the same set of filters for these two orientations, we may neglect important information in the frequency domain.

Phase symmetry (PS) estimation

After designing of $R_{s,o}(\omega)$ and $G_o(\phi)$, we can compute the local PS for k th frame according to the following equation:

$$PS_k(x, y) = \frac{\sum_s \sum_o (|P_{(s,o)}(x, y)| - |Q_{(s,o)}(x, y)| - T_o)}{\sum_s \sum_o \sqrt{P_{(s,o)}^2(x, y) + Q_{(s,o)}^2(x, y)} + \varepsilon}, \quad (6)$$

where $P_{(s,o)}(x, y)$ and $Q_{(s,o)}(x, y)$ are the quadrature outputs of the designed filter at scale s and orientation o , i.e., $P_{(s,o)}(x, y) = \text{real}(F^{-1}(F_{(s,o)}(\omega, \phi)) * U_k(x, y))$ and $Q_{(s,o)}(x, y) = \text{imag}(F^{-1}(F_{(s,o)}(\omega, \phi)) * U_k(x, y))$. Here, $F^{-1}(\cdot)$ indicates the inverse Fourier transform, $*$ represents the convolution operation and $F_{(s,o)}(\omega, \phi) = R_{s,o}(\omega)G_o(\phi)$. ε ($=0.0001$) is a small constant introduced to avoid division by

zero error. T_o is an orientation-dependent noise compensation term, and it represents the maximum response that could be generated from the noise alone in the signal. T_o is calculated from the local energy distribution assuming a flat frequency spectrum due to noise, i.e., $T_o = \mu + n\sigma$, where μ and σ are the mean and standard deviation of that distribution. n is a constant. μ and σ are estimated from the response of the above-mentioned special filter at each orientation because it gives us the largest bandwidth and strongest noise response. We estimate PS (Fig. 11) for the example US image, where high magnitude is observed at the simulated bone locations.

Bone response (BR) estimation

Since PS is expected to have high magnitude at symmetry locations, it also demonstrates high values at other features (e.g., soft tissue–muscle interface) in the US images [8]. Since our interest is mainly to enhance the bony anatomy in the image, we use the shadow information of each bone in the US image. To estimate the shadow responses, we have followed the idea proposed by Foroughi et al. [4]. In short, the shadow below an image pixel is estimated by weighted summation of the intensity values of all pixels beneath as follows:

$$SM_k(x, y) = \frac{\sum_{j=x}^H G(j, y) U_k(j, y)}{\sum_{j=x}^H G(j, y)}, \quad (7)$$

where $SM_k(x, y)$ is the estimated shadow map (SM) for pixel (x, y) at k th normalized US frame, x and y indicate the row and column indices of the US image, and H is the total number of rows of $U_k(x, y)$. $G(\cdot)$ represents the Gaussian weighting function that models the transition of high-intensity pixels near to the bone surface to the dark pixels deeper under the bone. The product of SM with PS is defined as the bone response (BR) ($BR_k(x, y) = PS_k(x, y) SM_k(x, y)$) value in our work. Since both $PS_k(x, y)$ and $SM_k(x, y)$ vary from 0 to 1, $BR_k(x, y)$ also has a range from 0 to 1.

Reduction in computational complexity

The above-mentioned filter design is proposed for a particular 2D US frame. Since our target is to estimate the bone locations in a 3D US volume, we need to estimate the filter parameters for each frame separately in order to get the bone locations in the 3D US volume, which leads to a time-consuming process. To reduce the computational complexity, we use the similarity information between the Fourier transformations (only magnitude) of the US frames. To do this, we choose a particular US frame $U_k(x, y)$ as a reference frame ($U_r(x, y) = U_k(x, y)$), design the filters and estimate the bone response $BR_k(x, y)$. Then, the next US slice

($U_{k+1}(x, y)$) is transformed into the Fourier domain, and its normalized correlation with the magnitude of the reference transform is computed. If the normalized cross-correlation is greater than a set threshold, such as 0.95 in this paper, then we use the previously estimated filter parameters, i.e., filter parameters estimated from the reference frame will be used. Otherwise, we recalculate the filter parameters for the $(k+1)$ -frame and consider it as a new reference. In this way, we can save significant computation time associated with the estimation of the filter parameters. For our case, we notice that we need to calculate filter parameters for only 10–15 frames among 123 frames of a typical 3D US volume which corresponds to a 88–92 % saving of computation time for a 3D US volume.

Registration of a statistical wrist model to US volumes

For development of the statistical wrist model, we use our previously published approach [21]. In short, a joint statistical model (shape, inter-pose and intra-pose models) of the wrist is based on the previous analysis of shape and pose variations of carpal bones across a group of subjects at different wrist positions. There are three sets of model coefficients corresponding to the three different models, i.e., shape ($^s\Theta$), inter-pose ($^p_1\Theta$) and intra-pose ($^p_2\Theta$) coefficients.

In order to register the model to a target wrist (given by a point cloud estimated from the bone response images), we use the approach published in our previous work [23, 28]. To construct the target point cloud, we use a simple thresholding with a threshold of 0.1 on the bone response images to detect the wrist bones in the US volume. Note that small variations in this threshold value can be compensated by the following probabilistic registration technique that is robust to outliers and missing points. For initialization of the wrist model to the target wrist, we use a landmark-based approach where transformation between a set of corresponding points in the model and target is used. The target point cloud is assumed to be an observation generated by a Gaussian Mixture Model (GMM), and an Expectation Maximization (EM) framework is applied to optimize the model parameters and perform the registration [28].

In short, we first compute the probability of how likely a point in the model generates another point from the target (z_n) in the expectation step:

$$P(t_l^m | z_n) = \frac{b_n \exp\left(-\frac{1}{2} \left\| \frac{z_n - \phi(t_l^m; ^s\Theta, ^p_2\Theta, ^p_1\Theta)}{\sigma} \right\|^2\right)}{\left\{ \sum_{l=1}^L \sum_{m=1}^M b_n \exp\left(-\frac{1}{2} \left\| \frac{z_n - \phi(t_l^m; ^s\Theta, ^p_2\Theta, ^p_1\Theta)}{\sigma} \right\|^2\right) \right.} \\ \left. + (2\pi\sigma^2)^{1.5} \left(\frac{w}{1-w}\right) \left(\frac{ML}{N}\right) \right\}} \quad (8)$$

where \mathbf{z}_n represents the n th point of the target point cloud, b_n represents the bone probability of the n th point of the target point cloud, \mathbf{t}_m^l is the m th point of the developed model belonging to the l th carpal bone, $\Phi(\cdot;^s \Theta, ^p \Theta, ^p \Theta)$ is an instance of the model generated using shape, inter-pose and intra-pose coefficients, L is the total number of carpal bones used, M is the total number of points per bone in the model, N is the total number of points in the detected point cloud, and w is a factor to account for outliers. σ is the standard deviation of the Gaussian components which is chosen to be large initially, and its value is decreased in each iteration. In the maximization step, the following objective function is minimized:

$$Q = \sum_{l=1}^L \sum_{m,n=1}^{M,N} P(\mathbf{t}_m^l | \mathbf{z}_n) \|\mathbf{z}_n - \Phi(\mathbf{t}_m^l;^s \Theta, ^p \Theta, ^p \Theta)\|^2. \quad (9)$$

The cost function is minimized alternately with respect to the model coefficients using the Quasi-Newton method.

Evaluation of the proposed approach

We evaluate our bone enhancement approach on US data acquired from two different wrist phantoms and two volunteer wrists by registering the statistical wrist model to the resulting enhanced bone surfaces. The results are further compared to the result of two previously published methods [8, 11] for bone detection in US images which we multiply by the shadow map to allow for a fair comparison. We report the best results obtained with the previous approaches [8, 11] through an exhaustive search in the parameter space. The phantom design follows the phantom construction procedure described in [16]. Additional ball bearings are included into the phantom to allow for the generation of a reference registration. 3D US volumes are acquired from the two phantoms and the left and right wrists at two different wrist positions of both volunteers. US scanning is performed in the sagittal planes of the palmar side of the wrist such that the scaphoid bone appears roughly in the center of the US volume. To obtain the US volumes, a motorized transducer (Ultrasonix 4D L14-5/38) with a field of view of 30.10° , an angular difference of 0.2447° between frames and a center frequency of 10 MHz is used. The size of the acquired US volume is $436 \times 480 \times 123$, equivalent to $40 \times 40 \times 40$ mm in physical dimensions. Figure 3a shows the position of the US transducer on the left wrist. The top, bottom, left and right positions of the transducer are also demonstrated in Fig. 3b. Although our primary interest is detection of the scaphoid bone in the US volume, we register an ensemble of wrist bones to improve the registration accuracy by allowing bone features of neighboring bones to be used in the registration

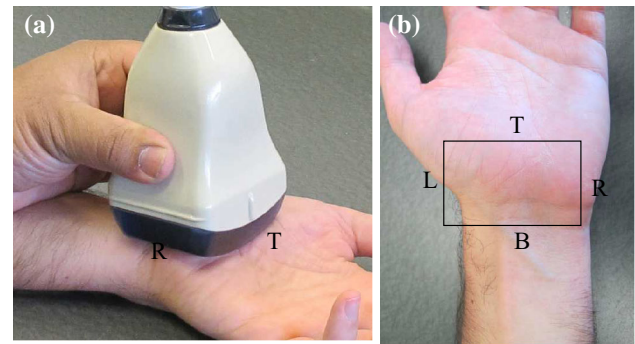


Fig. 3 Wrist scanning procedure. **a** Position of the US transducer on the wrist. **b** Schematic top (T), bottom (B), left (L) and right (R) positions of the US transducer on the left wrist

process. The relatively smooth and featureless surface of the scaphoid bone might otherwise result in an incorrect registration of the scaphoid bone to closely located carpal bones.

For quantitative evaluation, the registered model of the phantom data is compared with the reference surfaces, generated from a CT scan of the phantom. The reference surface for each carpal bone is generated by interactively segmenting the carpal bones in the CT volumes using the interactive segmentation plugin of the Medical Imaging Interaction Toolkit (MITK) [17]. We calculate the surface distance error (SDE) for each point of the registered surface by computing the average distance between all points on the registered surface and their closest neighboring points in the reference surface. The number of vertices for each registered bone surface is 1502, and the mean and standard deviation of these 1502 SDEs are computed to get the statistical moments of the calculated errors for each bone.

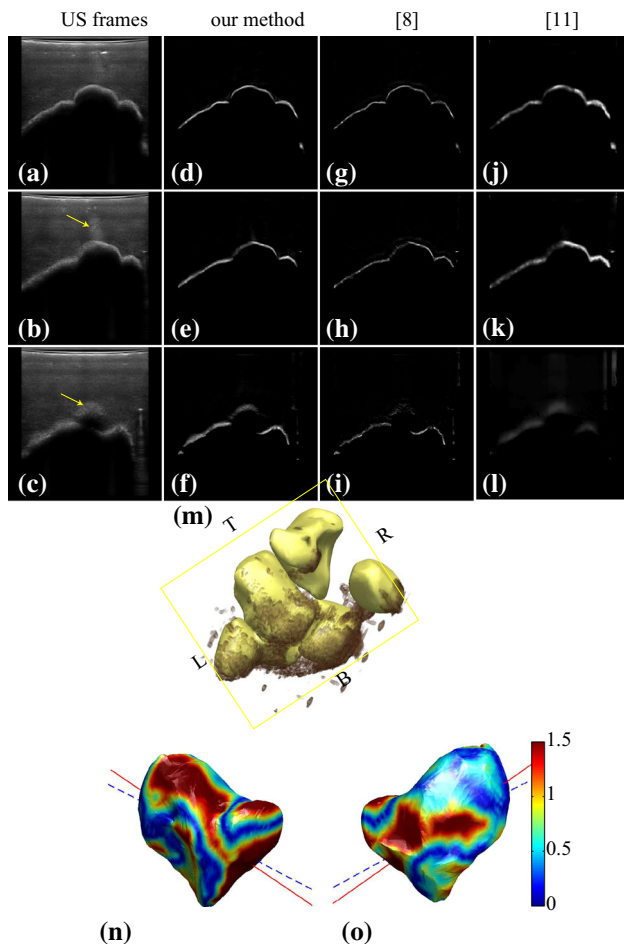
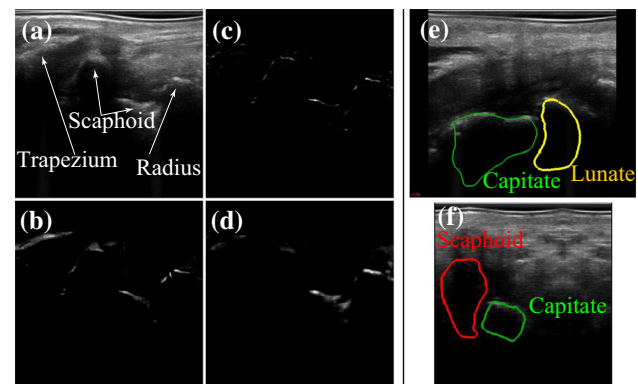
The accuracy in predicting the major axis of the scaphoid bone is determined as the error in deviation of the principal axis of the registered model and that of the reference surface of the scaphoid bone. We also measure the computation time for the bone enhancement technique and the registration of the wrist model to the enhanced US volume. The computation times are calculated from MATLAB code running on an Intel core-i7 3.40 GHz machine for both phantom and in vivo data.

Results

Table 1 shows the mean and standard deviation of SDE for the registration performed on the volumes acquired from the two wrist phantoms. For the five carpal bones, the accuracies are in the range between 1.00 and 1.21 mm compared to 1.22 to 1.41 mm and 1.11 to 1.27 mm for the methods presented in [8] and [11], respectively. Figure 4a–c shows three sample US images acquired from one of the wrist phantoms. Figure 4d–f, 4g–i and 4j–l show the BR images corresponding to US slices in Fig. 4a–c using our method, [8] and [11], respec-

Table 1 Mean and standard deviation of SDEs in mm computed from 1502 surface points for each of the five carpal bones for two wrist phantoms and comparison with [8, 11]

	SDE of 1st phantom (mean \pm sd)			SDE of 2nd phantom (mean \pm sd)		
	Our method	[8]	[11]	Our method	[8]	[11]
Scaphoid	1.04 \pm 0.56	1.31 \pm 0.67	1.11 \pm 0.58	1.11 \pm 0.59	1.29 \pm 0.71	1.15 \pm 0.60
Lunate	1.21 \pm 0.82	1.41 \pm 0.89	1.28 \pm 0.82	1.17 \pm 0.72	1.39 \pm 0.84	1.27 \pm 0.79
Capitate	1.02 \pm 0.47	1.24 \pm 0.62	1.11 \pm 0.52	1.09 \pm 0.51	1.22 \pm 0.59	1.17 \pm 0.54
Hamate	1.00 \pm 0.66	1.31 \pm 0.85	1.12 \pm 0.73	1.03 \pm 0.62	1.29 \pm 0.75	1.13 \pm 0.70
Pisiform	1.08 \pm 0.65	1.25 \pm 0.75	1.19 \pm 0.69	1.01 \pm 0.62	1.29 \pm 0.78	1.19 \pm 0.66

**Fig. 4** Results of the evaluation of the proposed approach with a wrist phantom and the comparison with [8] and [11]. **a–c** Three US images of the first wrist phantom. **d–f** Bone response images generated by our proposed method. **g–i** BR images generated by [8]. **j–l** BR images generated by [11]. The differences between the results are evident in the last US frame, where our presented method has shown advantages in the detection of blurred bone edges in the presence of artifacts compared to [8, 11]. The proposed method has enhanced the partially visible bone surface in **c** (marked by an arrow) that has not been noticed in **i**. **m** Overlay of registered wrist model to volume rendering of US volume acquired from the first wrist phantom. **n, o** Registered scaphoid surfaces at palmar and dorsal views. The color represents the error in mm of the registered surface with respect to the reference surface extracted from CT data. The major axes of the surfaces are shown for both the reference (straight line) and the registered model (dashed line)**Fig. 5** Registration results of the proposed approach for an example volunteer wrist. **a** An example US frame. **b** US bone responses enhanced by our proposed approach, **c** [8] and **d** [11]. **e–f** Overlay of registered atlas to US images

tively. Figure 4m shows the overlay of the registered wrist model to a volume rendering of US volume acquired from the first wrist phantom. Fig. 4n, o shows the registered scaphoid surfaces generated by our method for the palmar and dorsal sides, respectively. It also demonstrates the major axes computed from the registered and gold standard surfaces, marked by dashed and solid lines, respectively. The angle between the major axes of registered and ground-truth surfaces is computed for each wrist phantom using our method, [8] and [11]. The angular deviations between the major axes are 4.9° and 4.6° compared to 6.5° and 6.9° for [8], and 5.6° and 5.0° for [11], computed for the first and second wrist phantoms, respectively. For the in vivo data, example bone enhancements by our method and [8, 11] are demonstrated in Fig. 5a–d. Example registration results generated by our proposed technique are shown in Fig. 5e–f. The current computation times for the bone enhancement by our method, [8] and [11] of an US volume are 5:53 min, 0:55 min and 1:02 min, respectively. The computation time for the registration ranges from 2:04 min for 2500 target points to 8:41 min for 9000 target points. Note that the above computation times are the same for both phantom and in vivo data.

Discussion and conclusion

We have presented a novel bone enhancement approach for US images accounting for local spectrum variations and used it for registration of a statistical wrist model to allow for augmentation of the US image for guiding percutaneous interventions such as for scaphoid fracture fixation. The key novelty is to use adaptive filters for bone detection in US. Feasibility experiments have been performed on phantom and in vivo US data. We compared our results with two previously published approaches [8, 11]. The differences between the results are evident for the US frame in Fig. 4c, where our presented method has shown advantages in the detection of blurred bone edges and low-contrast bone surfaces compared to [8, 11]. The registration result observed in Fig. 4j indicates that the registered model using our proposed approach matches well with the partial bone surfaces in US. The mean SDE obtained with our method was found to be smaller than the surgical accuracy (2 mm). The major axis of the registered scaphoid bone has deviated by $<5.0^\circ$ from the reference axis. We could show for one in vivo case that our method is able to enhance blurred and disconnected bone surfaces and suppress responses not originating from bone surfaces. Although our method is computationally more expensive than the methods proposed in [8, 11], the presented bone enhancement approach shows promising results in enhancement of disconnected, blurry bone edges as well as in suppressing other non-bony features.

One of the limitations of our method is the segmentation of the local frequency responses ($p(\phi)$, $q_o(\omega)$). It may detect false minima in the response or if two maxima are too close, then it may detect them as one single maximum. As a result, the local spectrum will not be accurately segmented and subsequent local PS estimation will be less accurate.

Future studies should further include the evaluation of the approach on in vivo US data from fractured subjects. We believe that our current method can be directly applied to non-displaced fractured cases. For displaced fractured cases, an extension of our registration approach (e.g., by non-rigid registration) can be used to compensate the displacements of the fractured parts. Furthermore, it should be investigated whether acquisition of the US signal from the dorsal side of the wrist provides better image information on more challenging geometric viewpoints. Moreover, we aim to automate the initialization of the wrist model to the US volume. For use in a practical real-time guidance system, the runtime, which is currently within several minutes, needs to be substantially reduced. C++ implementation of the registration algorithm in a multiprocessor graphic processing unit can be used to substantially reduce the computation time. Efficient parallel implementation can be also applied to the bone enhancement for further reduction in the runtime. In conclusion, the presented US bone enhancement method has

demonstrated promising results in feasibility experiments and has the potential to find applications in a guidance system for orthopedic surgical procedures such as percutaneous scaphoid fracture fixation.

Declaration

The authors declare that they have no conflict of interest. All procedures performed in studies involving human participants were in accordance with the ethical standards of the institutional and/or national research committee and with the 1964 Helsinki Declaration and its later amendments or comparable ethical standards. This article does not contain any studies with animals performed by any of the authors. Informed consents were obtained from all individual participants included in the study.

References

1. Amin DV, Kanade T, Digioia AM, Jaramaz B (2003) Ultrasound registration of the bone surface for surgical navigation. *Comput Aided Surg* 8(1):1–16
2. Beek M, Abolmaesumi P, Luenam S, Ellis RE, Sellens RW, Pichora DR (2008) Validation of a new surgical procedure for percutaneous scaphoid fixation using intra-operative ultrasound. *Med Image Anal* 12(2):152–162
3. Clarke C, Moore J, Wedlake C, Lee D, Ganapathy S, Salbalbal M, Wilson T, Peters T, Bainbridge D (2010) Virtual reality imaging with real-time ultrasound guidance for facet joint injection: a proof of concept. *Anesth Analg* 110(5):1461–1463
4. Foroughi P, Boctor E, Swartz M (2007) 2-D ultrasound bone segmentation using dynamic programming. In: *IEEE ultrasonics symposium*, pp 2523–2526
5. Gilles J (2013) Empirical wavelet transform. *IEEE Trans Signal Process* 61(16):3999–4010
6. Gilles J, Tran G, Osher S (2014) 2D empirical transforms. wavelets, ridgelets, and curvelets revisited. *SIAM J Imaging Sci* 7(1):157–186
7. Grau V, Noble JA (2005) Adaptive multiscale ultrasound compounding using phase information. In: *Medical image computing and computer-assisted intervention-MICCAI 2005*. Springer, Berlin, pp 589–596
8. Hacıhaliloglu I, Abugharbieh R, Hodgson AJ, Rohling RN (2009) Bone surface localization in ultrasound using image phase-based features. *Ultrasound Med Biol* 35(9):1475–1487
9. Hacıhaliloglu I, Abugharbieh R, Hodgson AJ, Rohling RN (2011) Automatic adaptive parameterization in local phase feature-based bone segmentation in ultrasound. *Ultrasound Med Biol* 37(10):1689–1703
10. Hacıhaliloglu I, Abugharbieh R, Hodgson AJ, Rohling RN, Guy P (2012) Automatic bone localization and fracture detection from volumetric ultrasound images using 3-D local phase features. *Ultrasound Med Biol* 38(1):128–144
11. Hacıhaliloglu I, Rasoulia A, Rohling RN, Abolmaesumi P (2014) Local phase tensor features for 3D ultrasound to statistical shape+pose spine model registration. *IEEE Trans Med Imaging* 33(11):2167–2179
12. Jain AK, Taylor RH (2004) Understanding bone responses in B-mode ultrasound images and automatic bone surface extraction

- using a Bayesian probabilistic framework. In: Medical imaging, international society for optics and photonics, pp 131–142
13. Khallaghi S, Mousavi P, Gong RH, Gill S, Boisvert J, Fichtinger G, Pichora D, Borschneck D, Abolmaesumi P (2010) Registration of a statistical shape model of the lumbar spine to 3d ultrasound images. In: Medical image computing and computer-assisted intervention-MICCAI 2010. Springer, Berlin, pp 68–75
 14. Kovese P (1997) Symmetry and asymmetry from local phase. In: Tenth Australian joint conference on artificial intelligence, vol 190. Citeseer
 15. Kowal J, Amstutz C, Langlotz F, Talib H, Ballester MG (2007) Automated bone contour detection in ultrasound b-mode images for minimally invasive registration in computer-assisted surgery—an in vitro evaluation. *Int J Med Robot Comput Assist Surg* 3(4):341–348
 16. Madsen EL, Hobson MA, Shi H, Varghese T, Frank GR (2005) Tissue-mimicking agar/gelatin materials for use in heterogeneous elastography phantoms. *Phys Med Biol* 50(23):5597
 17. Maleike D, Nolden M, Meinzer HP, Wolf I (2009) Interactive segmentation framework of the medical imaging interaction toolkit. *Comput Methods Program Biomed* 96(1):72–83
 18. Meldon SW, Hargarten SW (1995) Ligamentous injuries of the wrist. *J Emerg Med* 13(2):217–225
 19. Menapace KA, Larabee L, Arnoczky SP, Neginhal VS, Dass AG, Ross LM (2001) Anatomic placement of the Herbert-Whipple screw in scaphoid fractures: a cadaver study. *J Hand Surg* 26(5):883–892
 20. Merrell G, Slade J (2008) Technique for percutaneous fixation of displaced and nondisplaced acute scaphoid fractures and select nonunions. *J Hand Surg* 33(6):966–973
 21. Mohammad Abu Anas E, Rasoulia A, John PS, Pichora DR, Rohling R, Abolmaesumi P (2014) A statistical shape+pose model for segmentation of wrist CT images. In: SPIE medical imaging, vol 9034, pp T1–T8
 22. Mink van der Molen A, Groothoff J, Visser G, Robinson P, Eisma W (1999) Time off work due to scaphoid fractures and other carpal injuries in The Netherlands in the period 1990 to 1993. *J Hand Surg Br Eur Vol* 24(2):193–198
 23. Nagpal S, Abolmaesumi P, Rasoulia A, Ungi T, Hacıhaliloglu I, Osborn J, Borschneck DP, Lessoway VA, Rohling RN, Mousavi P (2014) CT to US registration of the lumbar spine: a clinical feasibility study. In: Information processing in computer-assisted interventions. Springer, Berlin, pp 108–117
 24. Pao VS, Chang J (2003) Scaphoid nonunion: diagnosis and treatment. *Plast Reconstr Surg* 112(6):1666–1677
 25. Penney GP, Barratt DC, Chan CS, Slomczykowski M, Carter TJ, Edwards PJ, Hawkes DJ (2006) Cadaver validation of intensity-based ultrasound to CT registration. *Med Image Anal* 10(3):385–395
 26. Rahmatullah B, Papageorghiou AT, Noble JA (2012) Integration of local and global features for anatomical object detection in ultrasound. In: Medical image computing and computer-assisted intervention-MICCAI 2012. Springer, Berlin, pp 402–409
 27. Rajpoot K, Grau V, Noble JA (2009) Local-phase based 3D boundary detection using monogenic signal and its application to real-time 3-D echocardiography images. In: IEEE international symposium on biomedical imaging: from nano to macro, 2009 (ISBI'09). IEEE, pp 783–786
 28. Rasoulia A, Rohling R, Abolmaesumi P (2013) Lumbar spine segmentation using a statistical multi-vertebrae anatomical shape+pose model. *IEEE Trans Med Imaging* 32(10):1890–1900
 29. Smith EJ, Al-Sanawi HA, Gammon B, John PJS, Pichora DR, Ellis RE (2012) Volume slicing of cone-beam computed tomography images for navigation of percutaneous scaphoid fixation. *Int J Comput Assist Radiol Surg* 7(3):433–444
 30. Tran D, Rohling RN (2010) Automatic detection of lumbar anatomy in ultrasound images of human subjects. *IEEE Trans Biomed Eng* 57(9):2248–2256
 31. Yan CX, Goulet B, Pelletier J, Chen SJS, Tampieri D, Collins DL (2011) Towards accurate, robust and practical ultrasound-CT registration of vertebrae for image-guided spine surgery. *Int J Comput Assist Radiol Surg* 6(4):523–537